Journal of Vacuum Science and Technology A

RESEARCH ARTICLE | MAY 23 2023

Effect of tilted closed-field magnetron design on the microstructure and mechanical properties of TiZrNbTaN coatings

Special Collection: Celebrating the Achievements and Life of Joe Greene

Sanath Kumar Honnali ; Charlotte Poterie ; Arnaud le Febvrier ; Daniel Lundin ; Grzegorz Greczynski ; Per Eklund

Check for updates

J. Vac. Sci. Technol. A 41, 043402 (2023)
https://doi.org/10.1116/6.0002752

View Online
Export Citation
CrossMark

23 November 2023 11:57:08

JVST A
Journal of Vacuum Science & Technology A
ARTICLE
avs.scitation.org/journal/jva

Effect of tilted closed-field magnetron design on the microstructure and mechanical properties of TiZrNbTaN coatings

Cite as: J. Vac. Sci. Technol. A **41**, 043402 (2023); doi: 10.1116/6.0002752
Submitted: 7 April 2023 · Accepted: 5 May 2023 ·
Published Online: 23 May 2023

View Online Export Citation CrossMark

Sanath Kumar Honnali,[1,a)] Charlotte Poterie,[2] Arnaud le Febvrier,[1] Daniel Lundin,[3] Grzegorz Greczynski,[1] and Per Eklund[1]

AFFILIATIONS

[1]Thin Film Physics Division, Department of Physics, Chemistry, and Biology (IFM), Linköping University, Linköping 581 83, Sweden
[2]Faculty of Fundamental and Applied Sciences, University of Poitiers, Poitiers 86000, France
[3] Plasma and Coating Physics Division, Department of Physics, Chemistry, and Biology (IFM), Linköping University, Linköping 581 83, Sweden

Note: This paper is part of the Special Topic Collection Celebrating the Achievements and Life of Joe Greene.
[a)]**Electronic mail:** sanath.kumar.honnali@liu.se

23 November 2023 11:57:08

ABSTRACT

A common design of sputtering systems is to integrate many magnetron sources in a tilted closed-field configuration, which can drastically affect the magnetic field in the chamber and thus plasma characteristics. To study this effect explicitly, multicomponent TiZrNbTaN coatings were deposited at room temperature using direct current magnetron sputtering (DCMS) and high-power impulse magnetron sputtering (HiPIMS) with different substrate biases. The coatings were characterized by x-ray diffraction, scanning electron microscopy, nano-indentation, and energy dispersive x-ray spectroscopy. Magnetic field simulations revealed ten times higher magnetic field strengths at the substrate in single-magnetron configuration when compared to the closed-field. As a result, the substrate ion current increased ∼3 and 1.8 times for DCMS and HiPIMS, respectively. The film microstructure changed with the discharge type, in that DCMS coatings showed large sized columnar structures and HiPIMS coatings show globular nanosized structures with (111) orientation with a closed-field design. Coatings deposited from a single source showed dense columnar structures irrespective of the discharge type and developed (200) orientation only with HiPIMS. Coatings deposited with closed-field design by DCMS had low stress (0.8 to −1 GPa) and hardness in the range from 13 to 18 GPa. Use of HiPIMS resulted in higher stress (−3.6 to −4.3 GPa) and hardness (26–29 GPa). For coatings deposited with single source by DCMS, the stress (−0.15 to −3.7 GPa) and hardness were higher (18–26 GPa) than for coatings grown in the closed-field design. With HiPIMS and single source, the stress was in the range of −2.3 to −4.2 GPa with a ∼6% drop in the hardness (24–27 GPa).

© 2023 Author(s). All article content, except where otherwise noted, is licensed under a Creative Commons Attribution (CC BY) license (http://creativecommons.org/licenses/by/4.0/). https://doi.org/10.1116/6.0002752

I. INTRODUCTION

Magnetron sputtering is based on magnetic fields added to the direct current (DC) diode sputtering setup to increase the residence time of electrons near the cathode vicinity.[1,2] In a typical magnetron, this was achieved by arranging cylindrical magnets in concentric circles just behind the cathode. This type of arrangement enabled thin film deposition to operate at lower cathode voltage and working gas pressure with higher deposition rates compared to nonmagnetized DC diode sputtering.[3,4] Varying the magnetic field strength strongly influences the discharge properties such as deposition rate and flux of the sputtered species.[5] The magnetic configuration can be adjusted to improve the ion bombardment on the substrate and tune the film properties.[6,7] The modification done by strengthening the outer ring of magnets relative to inner magnets leads to *Unbalanced Type-II* configuration. This arrangement provides higher ion current densities of 5–10 mA/cm^2 at the substrate.[8] The polarities of the inner and outer magnets can be reversed and many such sources can be arranged alternatively.[9,10] Sproul *et al.*[11] studied such a dual-magnetron system with two sources with

© Author(s) 2023

opposed magnetic configuration with the substrate's rotation axis parallel to the magnetron surface. This type of arrangement increased the substrate bias-current densities compared to the mirrored dual-source configuration. The opposed field arrangement is known as *closed-field unbalanced magnetron* design, which results in significant ionization in the substrate vicinity.[12,13] The original geometry of alternating multiple magnetrons is still used commercially to deposit hard coatings in industrial grade systems.[14,15]

In a typical industrial closed-field unbalanced magnetron system, the magnetron surface is parallel to the substrate axes of rotation. However, when it comes to laboratory deposition systems, usually the magnetron surface is tilted at an angle to the substrate rotation axis either facing down[16] or up.[17] In DCMS, which is common in laboratory-based systems, the degree of ionization of the sputtered flux is around ∼0.1%[18] with ionization dominated by the Penning ionization process.[19] The ionization of the sputtered flux can be increased by applying high-amplitude pulsed power to the target with a low duty cycle. If the applied peak pulse power density is two orders of magnitude higher than the average power density, the technique is known as high-power impulse magnetron sputtering (HiPIMS).[20,21] This induces a higher electron density in front of the target that will ionize the sputtered atoms to a greater extent, through electron-impact ionization.[22] Since electrons have significantly smaller Larmor radius than the chamber dimensions, their transport will be influenced by the magnetic field. The ions follow the electrons to preserve the quasineutrality. Therefore, the modification of the magnetic field having either closed-field magnetrons or a single magnetron will affect the electron transport and thereby the ion transport to the substrate.

Rohde *et al.*[23] investigated the closed-field design in a dual-magnetron system with the substrate rotation axis parallel to the cathode surface. This design provided higher ion currents due to nonzero magnetic fields in the substrate vicinity. Engström *et al.*[16] reported a plasma coupling effect in a tilted closed-field dual magnetron laboratory system for the DC discharge. They added an external magnetic field at the substrate, which led to a change in crystallographic texture and densification of the film. Rao *et al.*[24] also reported the influence of the external magnetic field at the substrate on the phase formation, as well as composition of multicomponent (CrFeCoNi) nitride coatings in a tilted closed-field configuration with four magnetrons. Bohlmark *et al.*[25] used an external magnetic field at the substrate in a HiPIMS discharge with one magnetron to control the spatial distribution of ions and thus enhanced the deposition rate. It is clear from the previous instances that manipulating the magnetic field distribution in the chamber influences the film properties. However, if we consider four tilted sources with alternative magnetron configuration, the magnetic field lines from the outer magnets are coupled with the neighboring magnetrons.[9] This will trap the electrons that ionize the sputtered atoms and the ions in the vicinity of the target. Therefore, there is a need to understand and investigate the effect of the tilted design and, more specifically, the distribution of the magnetic field and their influence on DCMS and HiPIMS discharges.

To investigate this general research question, we choose TiZrNbTaN as a model system. DCMS of the TiZrNbTaN system has been investigated by Shu *et al.*[26] using two segmented targets. Coatings deposited below 400 °C exhibited *fcc* solid solution polycrystalline structures with a rough surface with a hardness of 26 GPa. Upon increasing the temperature (400–600 °C), the coatings developed a (001)-texture with dense structures without visible grain features with a 11% reduction in hardness. However, the same material system deposited by individual elemental targets on Si(100) at 400 °C shows a compressive stress of −1.5 GPa with a hardness of ∼28 GPa at −100 V bias.[27]

Sputtering of TiZrNbTaN with HiPIMS from a compound target at room temperature has not been reported to the best of our knowledge. HiPIMS discharge significantly increases the ionization of the sputtered species of TiZrNbTa alloy with various atomic sizes. The transport of these ions to the substrate is influenced by the magnetic field distribution in the chamber. The flux of ions reaching the substrate can be measured by applying a negative bias to the substrate and observing the bias current. This value is an indication of how efficiently the ions overcome the coupled magnetic field in a multiple magnetron design. This has implications on the film composition, which can lead to change in lattice parameter,[28] density,[29] and hardness[30] of the films. Therefore, it is crucial to understand the effect of the magnetron design before we look at the advantages of depositing TiZrNbTaN coatings using HiPIMS with an alloyed target.

In the present work, we report the simulation of the magnetic field in a specific deposition chamber and experimentally evaluate two different discharges (DC and HiPIMS) for the deposition of TiZrNbTaN coatings. The coatings were deposited either with four tilted magnetrons in a closed-field configuration with one active source and with single tilted source with different substrate biases in both cases. The crystal structure, morphology, composition, and mechanical properties of the coatings were investigated. We report a comparative analysis of the properties of coatings grown with DCMS and HiPIMS. We show that the magnetron arrangement in the chamber and the magnetic field distribution has a considerable effect on the film properties.

23 November 2023 11:57:08

II. EXPERIMENT

A. Film deposition

The TiZrNbTaN coatings were grown on polished Si(100) substrates of dimensions $10 \times 10\ \mathrm{mm}^2$ by reactive magnetron sputtering in an ultra-high vacuum chamber (base pressure $\sim 10^{-7}$ Pa). The deposition chamber has four magnetrons placed at a horizontal angle of 90° to each other. Each magnetron is tilted 30° to the substrate normal and configured as *Unbalanced Type-II*. The deposition system is described in detail elsewhere.[17] The polarities of the inner and outer magnets were flipped consecutively to have a closed-field configuration. For the single magnetron case, the other three magnetrons were replaced by flanges to seal their positions, and the remaining magnetron was configured with outer magnets having south (S) polarity up and inner ones having the north (N) polarity up (S–N–S). Coatings were deposited using either a four-magnetron closed-field (CF) design or a single magnetron (SM). The coatings deposited in the above configurations will be referred to as "DCMS_CF," "DCMS_SM" for DCMS and "HiPIMS_CF," "HiPIMS_SM" for HiPIMS discharge, respectively. The substrates were cleaned by acetone and ethanol in ultrasonic baths for 10 min and blown dry with N_2 gas. A 5.08 cm circular equimolar alloy

© Author(s) 2023

target of $Ti_{0.25}Zr_{0.25}Nb_{0.25}Ta_{0.25}$ (Plansee) was sputtered in a mixed Ar/N_2 atmosphere with a constant deposition pressure of 0.4 Pa (3 mTorr). The total gas flow rate ($Ar + N_2$) was kept at 67 SCCM with 85% Ar and 15% of N_2 (99.9% pure). Prior to each deposition, the target was sputter cleaned for 5 min in Ar (99.99% purity) atmosphere at 0.33 Pa (2.5 mTorr), otherwise at the same conditions used during deposition.

The coatings were deposited using two types of discharges: DCMS in power-controlled mode at 100 W and unipolar HiPIMS, in voltage-controlled mode (∼390 V) with a 50 μs pulse length (τ_{on}) and ∼20 A peak target current (I_{pk}). In HiPIMS, the pulsing frequency (f_{pulse}) was adjusted between 625 and 645 Hz to maintain an average power of 100 W during the depositions. The substrate holder was under constant rotation and without intentional heating throughout the deposition. For both discharge types, the substrate bias (V_{bias}) was changed from floating (∼−10 V) to various DC voltages of −50, −75, and −100 V.

The strength of the individual cylindrical magnets was measured using a Lakeshore 420 Gaussmeter. The magnetic field distribution in the deposition system was simulated by a home-built algorithm using the MAGPYLIB[31] package in Python and plotted using the MATPLOTLIB[32] package. The size, geometry of cathode arrangement, and magnetization (M) were used as the inputs to the simulation. Units of millimeter (mm), degree (°), and milli-Tesla (mT) were used for length, angles, and magnetization, respectively. The field was simulated by solving the Maxwell equation expressed through the magnetic scalar potential (ϕ_m) as $\mathbf{H} = -\nabla\cdot\phi_m$. The solution to this equation can be expressed by an integral over the magnetization distribution $\mathbf{M(r)}$ and is derived in Ref. 33. By inputting the integration volume value, a built-in function of the MAGPYLIB python package was used to calculate the field strength $\mathbf{B}$, in all three directions (B_x, B_y, and B_z).

B. Film characterization

X-ray diffraction (XRD) measurements were performed on the films with PANalytical X'Pert PRO diffractometer in Bragg–Brentano (θ–2θ) geometry with a Cu Kα (λ = 1.540 598 Å) radiation and Ni filter. The recorded 2θ range is 25°–90° with a step size of 0.001° and a time per step of 20 s. The residual stress, density, and pole figures measurements were performed using a Philips X'Pert MRD diffractometer. Pole figures were acquired with crossed slits ($2 \times 2\ mm^2$) as primary and parallel plate collimator as secondary optics, respectively. The stress in the films on the Si substrates is determined using the wafer curvature method by calculating the curvature of the Si substrate. Since it is a (100) cut wafer, a modified Stoney equation with biaxial modulus [$M_{(100)}$] value of ∼181 GPa[34] was used. The curvature was measured by performing a rocking curve on 004 peak of Si at different "x" locations along the substrate area. The measurement was performed using a hybrid mirror as incident optics and crystal analyzer with 0.125° slit. The density of the films was determined using x-ray reflectivity (XRR) with the same diffraction and incident optics as that of the stress measurements.

The cross-section morphologies of the films were observed by the scanning electron microscope (SEM, ∑IGMA 300, Zeiss) with an acceleration voltage of 2 kV. The metal elemental composition was obtained from energy dispersive x-ray spectroscopy (EDS, Oxford Instruments) at an acceleration voltage of 20 kV. The mechanical properties of the films were determined from nanoindentation (Hysitron Triboindenter TI 950). A Berkovich diamond tip with an aperture of 100 nm was used to perform 16 indentations, and the tip area function was calibrated using fused-silica reference sample. The films were indented with 1.5 mN load, which resulted in a maximum indentation depth of ∼50 nm. The hardness and elastic modulus data were obtained from the load vs displacement curves using the Oliver and Pharr method.[35]

III. RESULTS

A. Magnetic field simulations

Figure 1(a) shows the visualization of the coupled plasma in the deposition system due to CF. The plasma plume from the active magnetron is directed toward the adjacent magnetrons and little to no plasma emission is seen in the substrate position region marked as white patch. Figure 1(b) shows the picture of the discharge with single magnetron with the discharge directed to the substrate. Figures 1(c) and 1(d) depict the simulation of the magnetic field in the z direction with CF and SM, respectively. The white square at the top of Figs. 1(c) and 1(d) indicates the substrate holder position at 135 mm from the center of the magnetron arrangement. The width of the square is equal to the diameter of the substrate holder (50 mm). In Fig. 1(c), only two magnetrons are seen since the figure is a cross-section view cutting through opposite magnetrons both configured with a weaker inner magnet. We can observe that the magnitude of the magnetic field is zero ($|B| = 0$), forming a line between the pair of magnetrons along the z direction. The zero-field line extends up to the substrate and is a consequence of the closed field magnetron design with four sources. With the single magnetron, the field lines extend toward the substrate.

The plasma plume going to the adjacent magnetron, as seen in Fig. 1(a), can be better understood by looking at the top view of the B-field distribution. Figure 1(e) shows the distribution for CF just above the top of the tilted magnetrons. The width of the field line indicated the strength of the B-field. The simulation shows that the field lines are coupled with the adjacent magnetrons and correlate with the plasma plume seen in Fig. 1(a). The $|\mathbf{B}| = 0$ point is seen as a white area at the center between the four sources. In SM, the field lines are decoupled [Fig. 1(f)].

The algorithm was also used to retrieve the simulated magnetic field strength at the substrate with CF and SM. Figure 2(a) describes the magnetic field strength in the direction of the arrow at the substrate position as shown in Figs. 1(c) and 1(d). The red mark indicates the substrate size placed at the center of the substrate holder. In the closed-field case, the simulation indicated that the field lines are not directed toward the substrate and their strength equal to zero at the center. With a single magnetron, the field strength was higher with a value of $-50 \pm 4\ \mu T$. The negative sign indicates the direction of the magnetic field toward the single magnetron.

Figure 2(b) presents the time-averaged substrate bias current measured during film depositions due to positive ions ($\bar{I}_{bias} \approx I_{ion}$) reaching the substrate. With four sources, the ion current was measured to be 2.5 ± 0.05 mA and 5.5 ± 3 mA for DC and HiPIMS,

23 November 2023 11:57:08

© Author(s) 2023

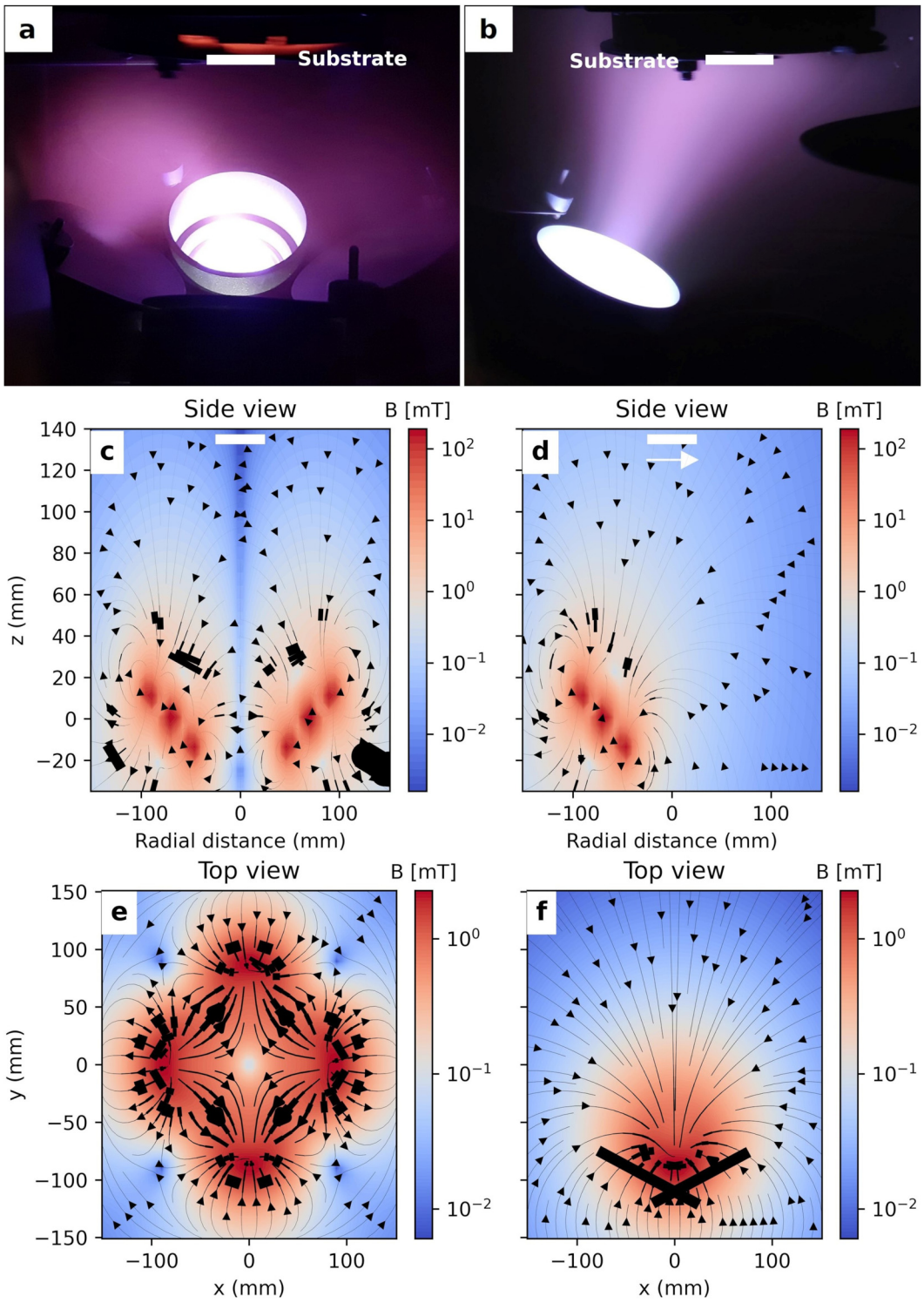

FIG. 1. Overview of the magnetically coupled plasma (a) with the three inactive magnetrons in closed field (CF) configuration and (b) without the inactive magnetrons in single magnetron configuration (SM). Magnetic field maps in the z direction toward the substrate in the log-10 scale in (c) CF and (d) SM configurations, respectively. Distribution of the magnetic field in the x–y plane in (e) CF and (f) SM configurations, respectively.

23 November 2023 11:57:08

© Author(s) 2023

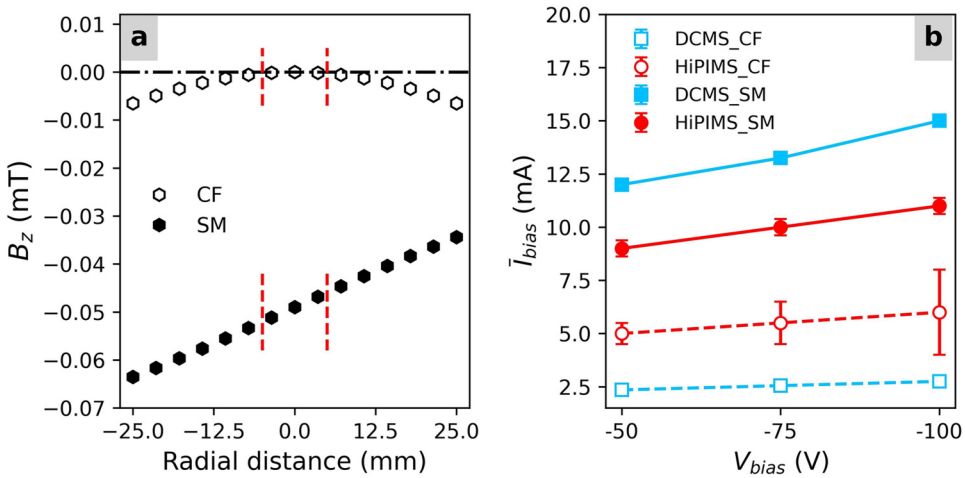

FIG. 2. (a) Simulated magnetic field strength at the substrate with closed-field (CF) and single magnetron (SM) configuration (the substrate position is indicated with the vertical red dashed line) and (b) the time-averaged bias current measured during depositions.

respectively. However, for the SM case with DC discharge, there was a three-fold increase in ion current to 13 ± 1.5 mA. For HiPIMS, the current rises ∼1.8 times higher to 10 ± 1 mA. The peak bias current was 298 ± 8 mA in the SM case just after the HiPIMS pulse. We can also observe fluctuations in $\bar{I}_{bias}$ values with HiPIMS_CF and the magnitude increase with substrate bias. In SM, the fluctuations were low compared to the CF case.

B. Film growth rate

Figure 3(a) displays the growth rate of TiZrNbTaN coatings as a function of the V_{bias}. The DCMS films were deposited for 75 min yielding a ∼500 nm thick coatings. The DCMS_CF had a deposition rate of 6.8 nm/min and the DCMS_SM follows the same trend but with a slower rate of ∼6 nm/min. For the HiPIMS films, the growth rate was ∼3 nm/min and independent of the number of magnetrons. The power-normalized growth rate in HiPIMS was half of the DCMS, mainly due to the back attraction of sputtered ions to the cathode.[36] Therefore, for obtaining thick films (∼500 nm), the deposition time was adjusted accordingly; however, thinner films were obtained.

C. Film composition

Figure 4 describes the variation in metal composition in the TiZrNbTaN coatings measured by EDS with discharge type and magnetron design. The statistical deviation in the measured composition of individual elements is not shown in the graph for easier interpretation. The deviation is around ∼1 at. % of the element composition. The broken lines indicate the film composition with a closed-field design and the solid line with single magnetron. The black dotted line indicates the equimolar target composition (i.e., 25 at. %). The data show that the individual metal content in the films varies with V_{bias}, discharge type, and number of magnetrons. For DCMS films [Fig. 4(a)], the Nb and Ta composition remained close to stoichiometry until −75 V bias and Ta changed at −100 V. The Ti content remained around ∼24 at. % and later dropped to 22 at. % for four and one magnetron, respectively. The Zr content in DCMS_SM films increased with the substrate bias and was the highest at −100 V with a value of ∼31 at. %.

For coatings deposited with HiPIMS, the composition drifted further from stoichiometry. Figure 4(b) shows that the HiPIMS discharge influenced the Zr and Ta composition, moderately on Ti and the least on Nb. It is important to note that the metals with similar masses (Zr, Nb) are higher in concentration, the heaviest (Ta) and lightest (Ti) among the four are lower for HiPIMS. However, the composition of the group 5 metals (Nb, Ta) remains close to the ideal concentration than group 4 (Ti, Zr) with DCMS.

23 November 2023 11:57:08

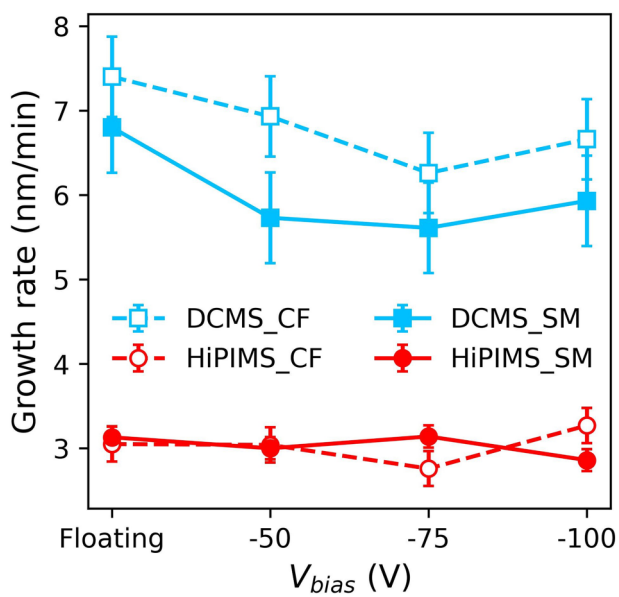

FIG. 3. Growth rate of TiZrNbTaN coatings deposited by DCMS and HiPIMS as a function of substrate bias.

© Author(s) 2023

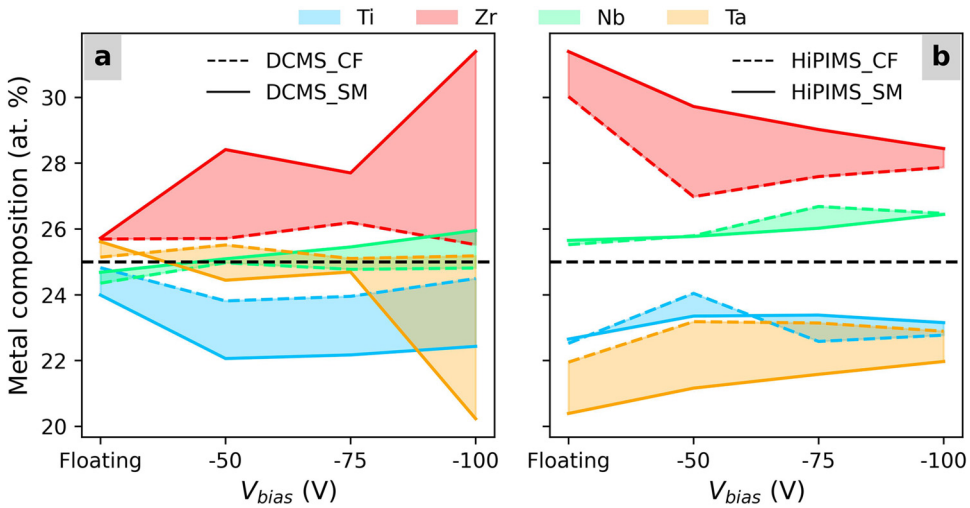

FIG. 4. Evolution of individual metal concentration (normalized) in TiZrNbTaN coatings with different magnetron designs (a) with DCMS and (b) with HiPIMS measured by EDS.

The detailed values of the individual metal composition with V_{bias} are shown in Fig. S3 See in the supplementary material.[62]

D. Crystal structure

Figure 5 shows the x-ray diffractogram of TiZrNbTaN coatings with intensity in the logarithmic scale. The XRD patterns of DCMS deposited films are shown in blue and those grown by HiPIMS are in red. The fading gradient indicates the increase in the magnitude of V_{bias}. The XRD pattern shows peaks at 2θ values of 35.37°, 41.07°, 59.47°, and 74.82° corresponding to 111, 200, 220, and 222 reflections from the NaCl-B1 type crystal structure. In DCMS_SM at −50 V bias, an asymmetric peak at $2\theta \approx 40°$ can be observed and consists of two peaks. Peaks marked with an asterisk (*) in red at $2\theta \approx 39.6°$ and 87.5° were identified as the 200 and 400 reflections from ZrN, respectively. The average lattice parameter (a) of 4.45 ± 0.02 Å (Fm-3 m) was calculated from the 111 and 200 peaks. The variation in lattice parameter with V_{bias} and discharge type is shown in Fig. S2(a) in the supplementary material.[62]

23 November 2023 11:57:08

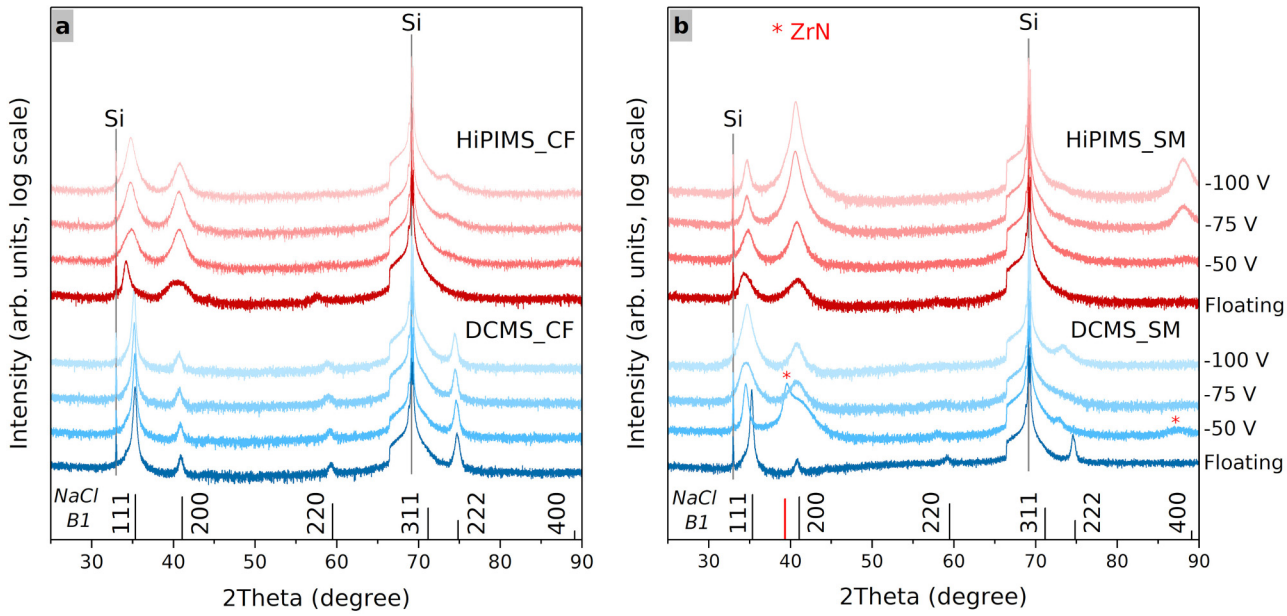

FIG. 5. XRD patterns of TiZrNbTaN coatings deposited at different substrate bias voltages using DCMS and HiPIMS: (a) closed field and (b) single magnetron. The NaCl B1 reference is based on the theoretical powder diffraction pattern of TiZrNbTaN.[26] The ZrN (200) reference was obtained from ICDD powder diffraction file number 00-035-0753.

© Author(s) 2023

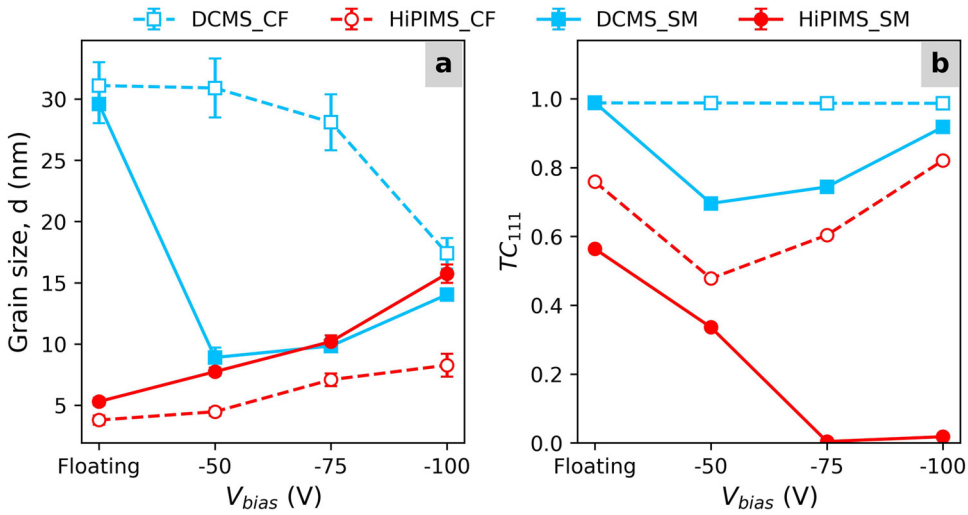

FIG. 6. (a) The average grain size as a function of bias. (b) The texture coefficient ratio of the TiZrNbTaN coatings as a function of substrate bias calculated using the 111 and 200 reflections.

In the DCMS_CF films, the 111-peak was the most intense the peak position did not shift with increase in V_{bias}. But, for HiPIMS_CF and DCMS_SM films, the peak position varied with applying V_{bias} and was lower than the theoretical values. For HiPIMS_SM films, large peak shift to lower 2θ values was observed for 111 peaks at floating bias. However, by applying bias, the difference between the observed peak position and the theoretical values became reduced. There was only small difference (Δ2θ ~0.04°) in the peak position at higher biases (−75 and −100 V) than peak at −50 V. The width of the XRD peaks varies significantly with V_{bias} and the discharge type. The crystallite domain microstrain contributes to the peak broadening. The Williamson–Hall method[37] was used to separate the broadening effect due to strain and the average grain size was calculated. Figure 6(a) describes the evolution in grain size "*d*," i.e., the coherently scattering domain size in the out-of-plain direction as a function of V_{bias}. In DCMS_CF films, the grain size reduced from 30 to 16 nm with an increased V_{bias}. For DCMS_SM films, the size sharply fell from ~30 to 10 nm from floating to −50 V and increased around ~4 nm at higher V_{bias}. The grain sizes of HiPIMS_CF films comprised between ~4 and ~8 nm, which is smaller than HiPIMS _SM (~5 to 16 nm). Note here that the trend in the grain size with V_{bias} is reversed for HiPIMS.

The relative intensity of the diffraction peaks varies depending on the number of magnetrons used revealing the changes in the film preferential orientation. The texture coefficient (TC), which is a measure of the degree of preferred orientation, for the films was calculated using the equation[38]

$$\mathrm{TC}\ (hkl) = \frac{I\ (hkl)/I_o(hkl)}{\frac{1}{N}\sum_N I\ (hkl)/I_o(hkl)}, \tag{1}$$

where "*I*" is the measured intensity of each (*hkl*) peak, I_o is the theoretical relative intensity,[26] and *N* is the number of peaks considered. In the above calculations, only the two most intense peaks (*N* = 2), i.e., 111 and 200 were considered. Figure 6(b) shows the ratio of the texture coefficient of 111. This means that the film contains entirely (111) textured grains; the texture coefficient ratio would be equal to 1 and will be equal to 0.5 for the film containing fully randomly oriented grains. The DCMS_CF films exhibited (111) preferential orientation. However, in HiPIMS_SM films, the 200 peaks became more intense compared to the 111 peaks when the bias was increased, and the TC ratio tends to zero.

Since DCMS_SM and HiPIMS_CF show a similar trend in preferred orientation with V_{bias} and to understand the nature of the additional peak, pole figures of 111 and 200 reflections of DCMS_SM films were acquired [Fig. 7(a)]. DCMS_SM films showed a 111 oriented growth at floating bias, no orientation with −50 and −75 V bias and 111 orientations at −100 V. The additional peak observed in XRD pattern is also visible as a pole at the center in addition to the TiZrNbTaN film ring at −50 V bias. This confirms that the additional peak is from the ZrN (200) planes. For HiPIMS_SM, at low bias voltages, no clear diffraction spot was observed in pole figures of 111 and 200 reflections [Fig. 7(b)]. However, when the bias was increased, a ring pattern started to develop in the 111 reflection and a spot at the center in the 200 reflections, respectively. Coatings grown at −100 V bias exhibited a sharp diffraction spot at the center observed in the 200-pole figure and a distinct ring at ψ ≈ 54.0° in the 111-pole figure. By applying bias, the crystalline quality improved and the films developed fiber-texture with (001) out-of-plane preferential orientation. The 111 peaks still seen in Fig. 5(b) is enhanced due to the logarithmic scale.

E. Cross-section morphology

Figure 8 shows the cross-section morphology of the TiZrNbTa nitride coatings. The thickness of the films varied with the V_{bias} and number magnetrons. The DCMS_CF films deposited in the floating condition exhibited columnar growth, with a column width around ~35 nm. The columns are slightly tilted due to the geometry of the magnetron [Fig. 8(a)]. The HiPIMS_CF films exhibited globular nanocrystalline

23 November 2023 11:57:08

© Author(s) 2023

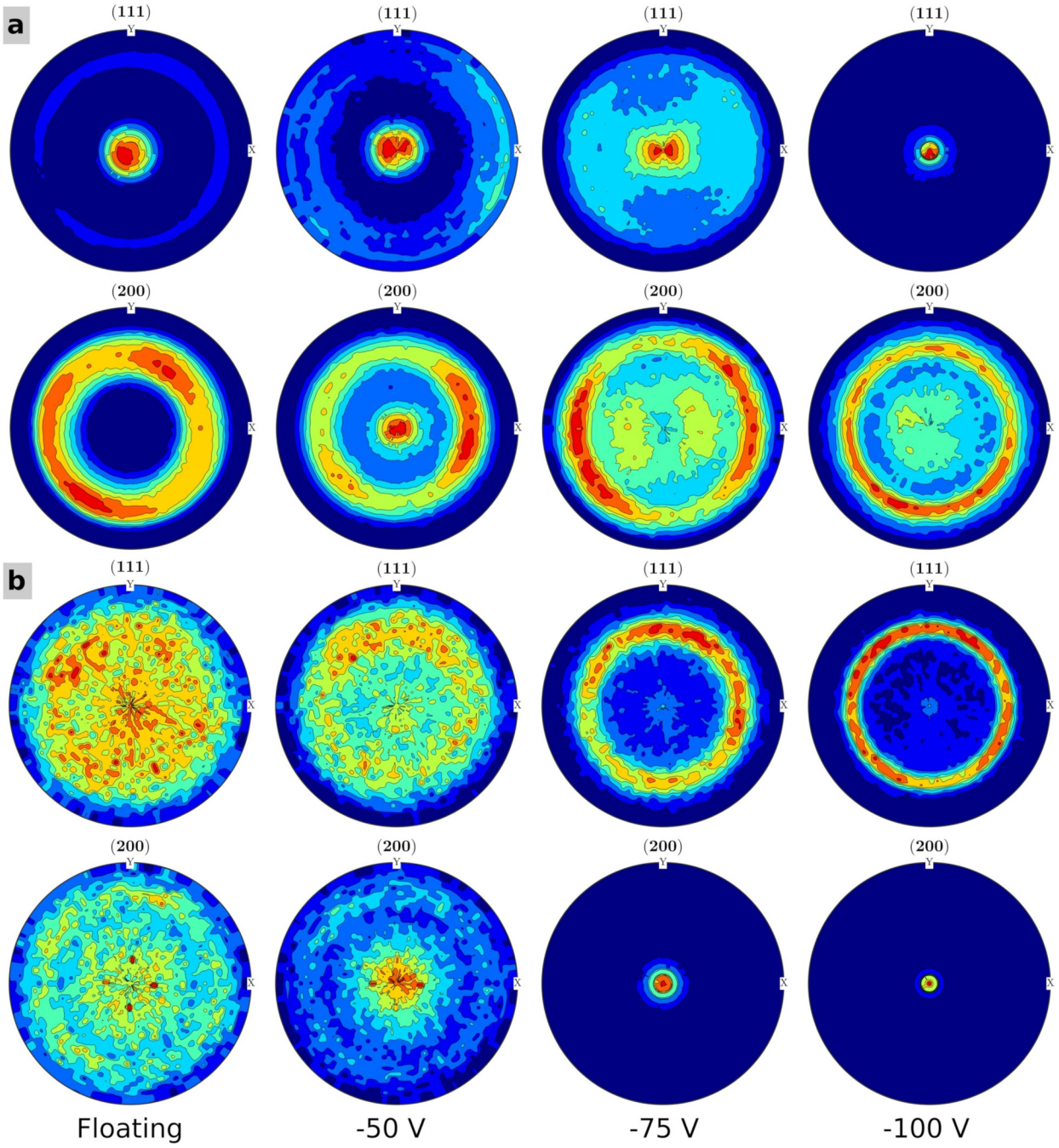

FIG. 7. Evolution of {111} and {200} pole figures of fcc TiZrNbTaN coatings deposited on Si (100) substrate at different bias voltages (a) for DCMS and (b) for HiPIMS both having single magnetron.

microstructure, which are less visible [Fig. 8(b)]. However, the columnar structure was retained in DCMS_SM [Fig. 8(c)], which densified as the bias was increased with smaller column widths.[39] For HiPIMS_SM [Fig. 8(d)] at higher biases, changes in the microstructure were observed, which may be due to the crystallographic fiber texture. It is worth noting that the columns grow normal to the substrate surface [Figs. 8(c) and 8(d)]. The thickness of the coatings is listed in Table I.

23 November 2023 11:57:08

© Author(s) 2023

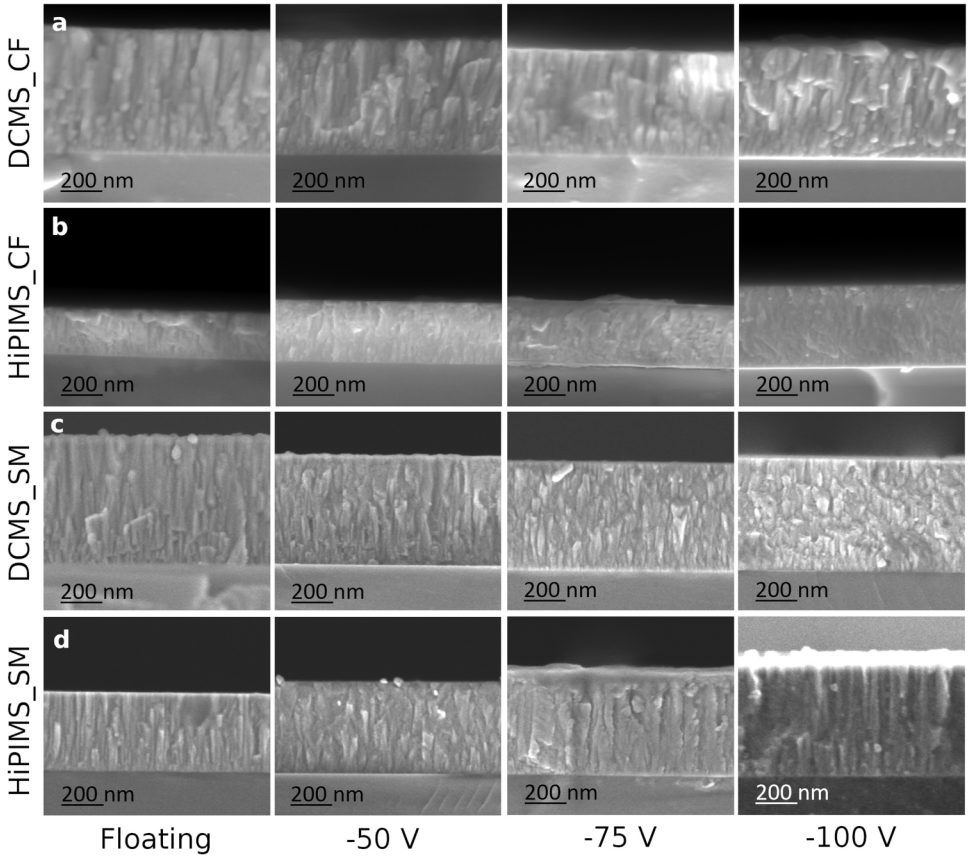

FIG. 8. Cross-sectional SEM images showing morphology of TiZrNbTaN coatings deposited by (a) DCMS_CF, (b) HiPIMS_CF, (c) DCMS_SM, and (d) HiPIMS_SM configuration as a function of substrate bias.

23 November 2023 11:57:08

TABLE I. Summary of the measured properties of TiZrNbTaN coatings on the Si(100) substrate.

	Substrate bias (V)	Critical size d_c (nm)	Film thickness (±10 nm)	Hardness (±1 GPa)	Residual stress (GPa)
DCMS_CF	Floating	~29	555	13.2	0.8 ± 0.6
	−50		520	16.4	−0.3 ± 0.2
	−75		470	15.8	−1 ± 0.1
	−100		500	18.1	−0.8 ± 0.1
HiPIMS_CF	Floating	~17	275	26.2	−3.6 ± 0.4
	−50		350	27.4	−4 ± 0.1
	−75		360	28.1	−4.3 ± 0.2
	−100		475	28.9	−4.2 ± 0.3
DCMS_SM	Floating	~17	510	18.1	−0.2 ± 0.1
	−50		430	26.1	−2.1 ± 0.1
	−75		421	25.4	−3.3 ± 0.2
	−100		445	26.8	−3.7 ± 0.2
HiPIMS_SM	Floating	~18	282	24.6	−2.3 ± 0.1
	−50		345	25.8	−2.7 ± 0.1
	−75		408	26.6	−3 ± 0.1
	−100		415	27.1	−4.2 ± 0.1

© Author(s) 2023

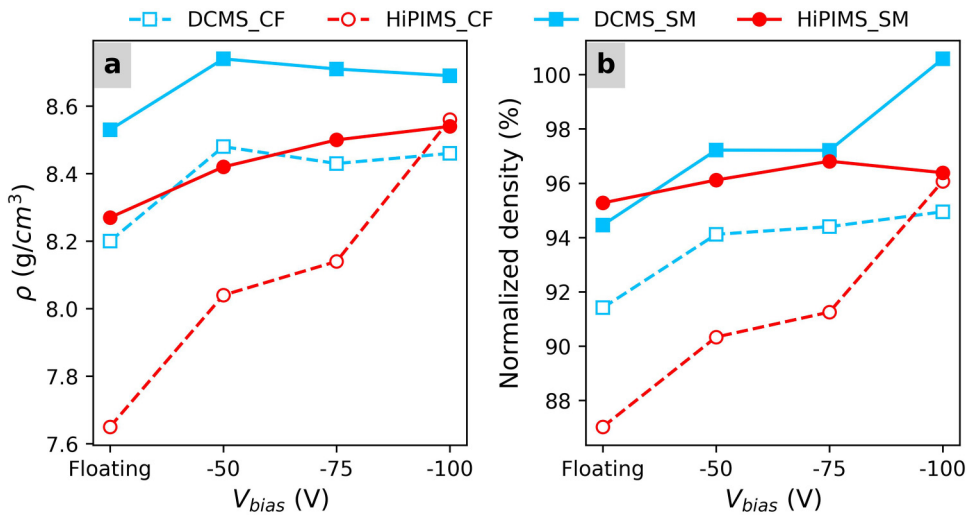

FIG. 9. (a) Density of the TiZrNbTaN coatings deposited by DCMS and HiPIMS with respect to the substrate bias found by x-ray reflectivity. (b) Normalized density of the films.

F. Film density

Figure 9(a) presents the film density of TiZrNbTaN coatings measured by x-ray reflectivity (XRR). The DCMS grown films had a common trend in density with applying bias. The DCMS_CF films undergo small densification with −50 V bias and remain constant (8.2–8.5 g/cm^3) thereafter. The DCMS_SM coatings were the densest and the values (i.e., ∼8.7 g/cm^3) were within the calculated density range. For HiPIMS_CF, the films were under-dense (7.6–8.1 g/cm^3) up to −75 V bias. However, at −100 V, the density increased to 8.6 g/cm^3 close to the calculated lower bound. For HiPIMS_SM film, the density increased steadily (8.3–8.5 g/cm^3) with bias but lower than the DCMS_SM film. Theoretical densities of the films were calculated from measured relaxed lattice constants and film compositions. Figure 9(b) represents the normalized density, i.e., the ratio of measured density to the calculated density in percentage at different V_{bias}. The density values measured from XRR were lower than the calculated values except for the DCMS_SM film at $V_{\text{bias}} = -100$ V, indicating a fully dense film. The higher measured density value at −50 V may be due to the additional ZrN phase. DCMS_CF and HiPIMS_CF had density differences of 6%–8% and 5%–13% from the calculated densities, respectively. With single magnetron, the differences in density values were reduced from ∼3% to ∼5%.

G. Mechanical properties

The DCMS_CF film exhibited a hardness between 13 and 18 GPa as shown in Fig. 10(a). The hardness of DCMS_SM with floating bias was 18 GPa and increases to ∼26 GPa with a bias of −100 V, which is a 55% increase compared to DCMS_CF. However, for HiPIMS_CF films, the hardness steadily increased to 28.85 GPa in a linear fashion from 26.2 GPa. For the HiPIMS_SM

23 November 2023 11:57:08

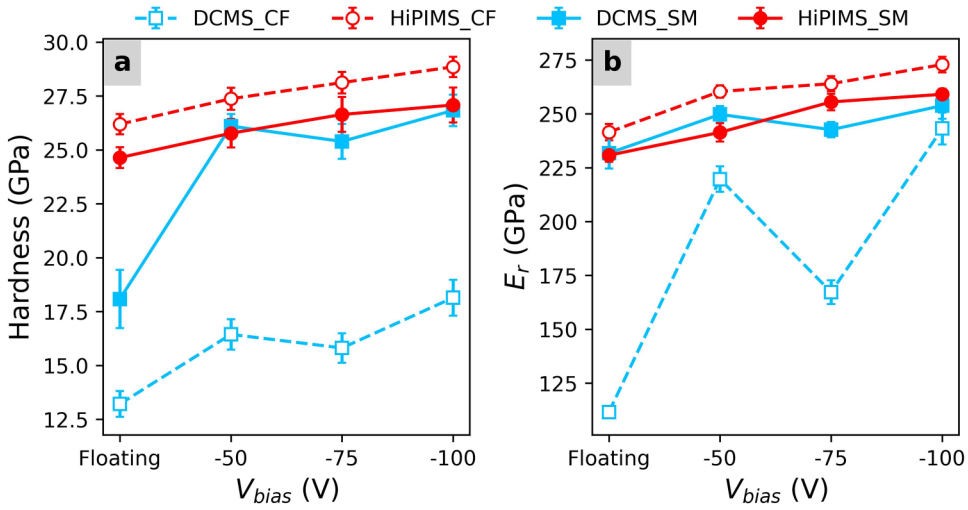

FIG. 10. (a) Hardness, (b) reduced elastic modulus of TiZrNbTaN coatings as a function of substrate bias.

© Author(s) 2023

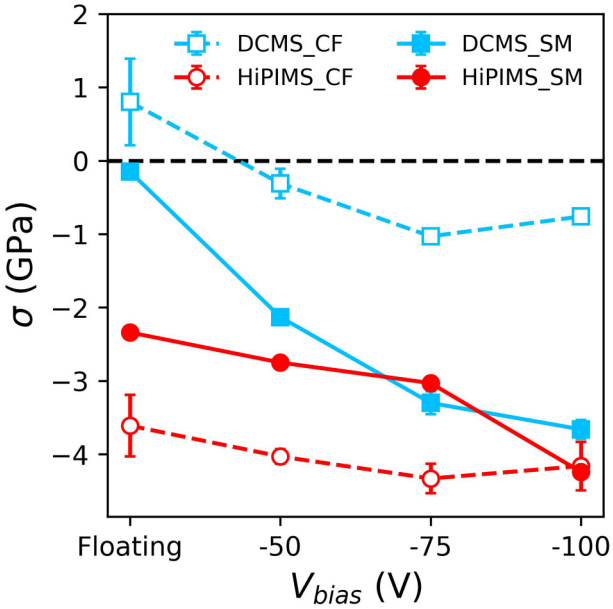

FIG. 11. Residual stress in TiZrNbTaN coatings deposited by DCMS and HiPIMS as a function of substrate bias.

case, the hardness followed a similar trend compared to HiPIMS_CF with a ~5.8% reduction in hardness.

The reduced elastic modulus (E_r) of the films is shown in Fig. 10(b). For DCMS_CF films, the values are 112 GPa for floating potential up to ~243 GPa for −100 V with an oscillatory behavior. For the films deposited in DCMS_SM, the reduced elastic modulus values were higher than DCMS_CF but still oscillatory with a lower amplitude between 231 and 253 GPa. For HiPIMS_CF deposited films, the modulus increased with bias linearly from 242 to 273 GPa. In the HiPIMS_SM film, the reduced young modulus followed the same trend as the one from the HIPIMS_CF films but with a lower modulus value (231–259 GPa). With one magnetron, the elastic modulus of the coatings is of the same order, irrespective of the discharge type.

H. Residual stress

Figure 11 shows the residual stress in the TiZrNbTaN coatings as a function of bias. With floating bias, the DCMS_CF films had a tensile stress around 0.8 GPa. When applying negative bias, the stress became compressive reaching a high value of −1 GPa. The stress of DCMS_SM had a similar trend as DCMS_CF but with higher stress values between −0.15 and −3.66 GPa. For HiPIMS deposited films, the stress followed the same trend with substrate bias linearly until −75 V. The HiPIMS_CF films exhibited compressive stress values between −3.6 and −4.3 GPa and for the HiPIMS_SM films between −2.3 and −3.0 GPa, respectively. However, at −100 V bias, there was a shift in the stress trend irrespective of the discharge type and number of magnetrons.

IV. DISCUSSION

With a closed-field design of four magnetrons, the electrons gyrate along the field lines connecting the adjacent magnetron as shown in Fig. 1(e). This is because all four magnetrons are *unbalanced Type-II*. The outer magnet rings are stronger and tend to couple toward the adjacent magnetron's field of opposite polarity [Fig. 1(e)]. Ionization occurs in the magnetic trap close to the target and the ions tend to follow the magnetic field lines due to electron trapping along the very same field lines.[25] Figure 2(a) shows the magnetic field lines close to the sources [Fig. 1(e)]. This confined B-field configuration in the near cathode region effectively limits ion transport to the substrate, as reflected in the observed bias currents [Fig. 2(b)]. When using the SM configuration, the field lines are directed toward the substrate [Fig. 1(d)], and one would expect a higher ion flux at the substrate, in agreement with the observed increase of the bias current [Fig. 2(b)]. In DCMS,

23 November 2023 11:57:08

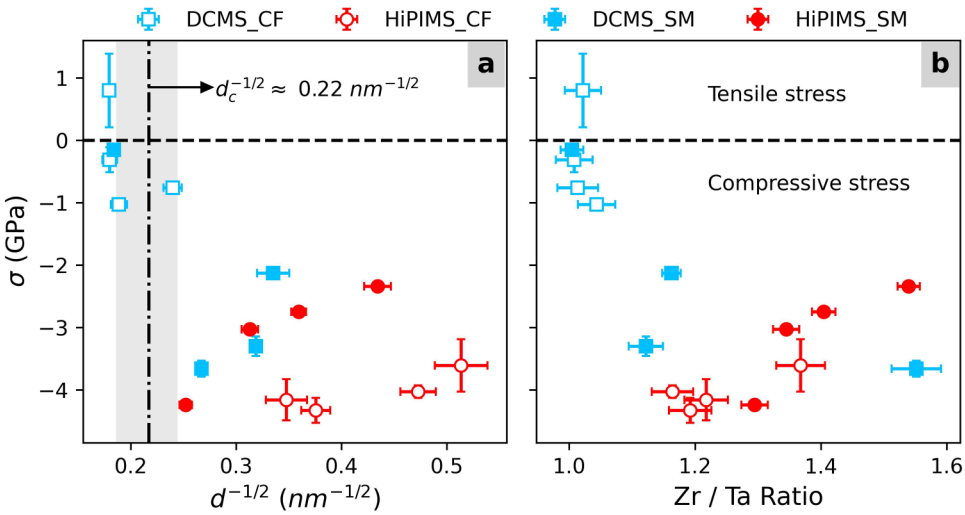

FIG. 12. Residual stress in TiZrNbTaN coatings as a function of (a) inverse square root of the grain size and (b) Zr to Ta composition ratio.

© Author(s) 2023

most of the sputtered species are neutral and the observed increase in bias current is due to gas ions. However, in HiPIMS, the sputtered species are ionized by the higher electron density generated due to the high-power density applied to the target. This leads to higher instantaneous bias currents at the substrate. The lower bias current observed in HiPIMS_CF is due to the magnetic trapping of the ions which may have facilitated the back attraction of the metal ions, than in the SM configuration.

The increase in bias current in HiPIMS deposited films influenced the film mass deposition rate (R_d). R_d is the amount of material being deposited per unit time per unit square centimeter area on the substrate. For the DCMS case, R_d exhibited a decreasing trend similar to the growth rate. The decrease in the growth rate of DCMS_SM with increasing V_{bias} is attributable to the densification and possibly to some extent also resputtering of the coating by ion bombardment.[40,41] But for HiPIMS, R_d increased with V_{bias} from $\sim 5 \times 10^{-8}$ to $\sim 9 \times 10^{-8}$ g/cm^2/s. This increased material flux contributed to the higher density of the films (Fig. 9), and hence the growth rates were similar for HiPIMS (Fig. 3).

The increase of the ion bombardment also induces lattice distortion[42] and a change in crystal orientation.[43] The lattice parameter varied between 4.44 and 4.48 Å and is shown in Fig. S2 in the supplementary material.[62] This variation was within the boundary of individual binary nitrides: 4.24 Å (TiN) and 4.61 Å (ZrN). The change in orientation from (111) to (001) was observed in HiPIMS_SM. The preferred orientation of the film depends on the overall energy condition with the contributions from strain and surface energies. For (001) orientation, the surface energy is the minimum and the strain energy will be the highest compared to the (111) plane.[44] The strain energy depends on the energy, ion flux, thickness of the film, and anisotropy in the material.[45] Since the ion energy are the same for both HiPIMS_CF and HiPIMS_SM films at any given substrate bias, the increase in strain energy due to larger ion flux may have induced the (001) orientations.

The additional peak of ZrN (200) observed in Fig. 5(b) have a d-spacing of 2.27 Å. These values are different than those observed for the TiZrNbTaN 200 peak and have different peak widths (FWHM). The compositional analysis also shows that the Zr content increases with depletion in Ti. Therefore, formation of a ZrN phase is possible due to the low Gibbs free energy of formation of ZrN (−367.3 kJ/mol[46]) compared to Ti, Nb, and Ta nitrides. If we look at the effect on the composition for HiPIMS_SM films, they have a reduced Ta content with an increase in the Zr content and vice versa for HiPIMS_CF. This means that with a closed-field case, it is more likely that a large fraction of Zr ion flux is back attracted by the target.

The lattice contraction observed in Fig. S2(a) in the supplementary material[62] can also be due to the compressive stress in the films. Chason *et al.*[47] reported that the stress generation was due to three factors: (a) during film growth, (b) substitution of atoms near grain boundaries, and (c) embedding of defects into grain volumes. The last two factors depend on the grain size and were proposed in the extended kinetic model. The dependence of stress in TiZrNbTaN films on the grain size is shown in Fig. 12(a), with the grain size converted to the inverse square root of the actual grain size. This was done to linearize the relation between stress, hence smaller values of $d^{-1/2}$ imply larger actual grain size (d). The DCMS_CF films had a larger grain size (∼30 nm) and varied only around ∼10% which results in low stress values (<−1 GPa). For the DCMS_SM films, the compressive stress linearly increases as the grain size becomes smaller. The trend is in good agreement with previous studies of TiN[48] and ZrN[49] films.

The films had lower stress with grain size larger than a threshold value shown in vertical dashed line and vice versa. The threshold grain size at which the hardness of the coating is maximum is known as the critical grain size (d_c).[50,51] The critical size was calculated using the dislocation pile up model, by assuming that the dislocation movement halts with only two dislocations piling up at ultralow grain sizes.[52] Using the above assumption, we can theoretically estimate the critical size using the modified Eshelby equation[53]

$$d_c = \frac{2nGb}{K\pi\tau}, \tag{2}$$

where G is the shear modulus which is equal to $E/2(1+\nu)$, where E is elastic modulus, ν is Poisson ratio, n is number dislocations in pile up (2, assumed), b is the magnitude of burgers vector ($b = \sqrt{2}*a\ /2$), K is a constant equal to $(1-\nu)$ and τ is critical shear stress. The plastic deformation occurs when $\tau = 0.5\ Y$, where Y is yield stress. The yield stress is equal to one third of the hardness value when considering plastic deformation in nitride films.[54] The critical size is material dependent[55] and varies with the composition of the film. By considering the elastic constant values of individual metal nitrides for a stochiometric film, the critical grain size was calculated to be ∼21 nm. The deviations in composition were considered, and the boundary values are shown as vertical shaded area in Fig. 12(a). The Zr and Ta content in the films were most affected; therefore, we express the change in residual stress as a function of Zr to Ta composition ratios in Fig. 12(b).

In DCMS_CF films, the Zr and other elements content was close to stoichiometry (25 at. %) and the stress values are low. The transition to compressive stress was due to gas ion bombardment. The transition occurred only after the critical grain size which was previously observed in sputtered TiN films.[48] The enhancement in compressive stress in DCMS_SM films was due to two factors: (i) the "ion peening effect" by an increased energetic gas ion bombardment;[56,57] (ii) the generation of defects from gas ion bombardment.[58] The enhanced bombardment altered the lattice spacing with a change in film composition having higher Zr content and reduction in Ti and Ta at −100 V [Fig. 4(b)]. These led to strain in the films due to the atomic size difference of Ti, Ta, and Zr atoms. The high and constant compressive stress with V_{bias} values for HiPIMS_CF films were the result of nanosized grains (<9 nm). This may be related to a constant Zr/Ta ratio than in DCMS_SM films. In HiPIMS_SM, the stress increases with the grain size and depletion of Zr, and the depletion increases with V_{bias}. This depletion is due to the resputtering of the film due to the increase in energy of metal ions reaching the substrate. However, coatings by HiPIMS_SM had larger grains (∼16 nm) due to increase in Nb and Ta contents, which densified films with reduced the number of defects.[48,58] Therefore, a clear relaxation of the stress was observed until −75 V bias. For grain sizes higher than the upper limit of d_c, the films were close to stress free. For sizes smaller than d_c, the

23 November 2023 11:57:08

© Author(s) 2023

films were found to have high stresses. This can be a crucial result for deciding the deposition parameters such as substrate bias, the peak current in HiPIMS.

Figure 13(a) describes the relation between the inverse square root of the grain size and the hardness of the TiZrNbTa nitride coatings. The dashed dot vertical line indicates the inverse square root of the critical grain size (d_c). For DCMS deposited films the hardness increased when the grain size became smaller until the critical grain size. However, for the HiPIMS films, the grain size was smaller than the critical size and the hardness increased with the grain size increase. The first phenomenon of hardness is known as the Hall–Petch effect and the latter one is the inverse Hall–Petch effect. The DC sputtered films obey the Hall–Petch relation until d_c, which states that the film strengthens with a decrease in the grain size.[59] The transition to inverse Hall–Petch is a function of the grain size and is observed only below the critical size (d_c), which is material specific.

The hardness in physical vapor deposited coatings is dependent on the factors such as grain size, density, composition, texture, and intrinsic stress.[49] In the present study, the DCMS_CF films were the softest of all films. The texture coefficient, density, and composition did not vary much with V_{bias}. Therefore, these factors do not influence the hardness. The observed small increment in hardness may be due to the minor increase stress values. The HiPIMS_CF films were the hardest among the films in the present study. A ~11% increase in hardness was observed with increasing the bias due to the presence of a strong {111} texture, increase in density, and high stress.

The DCMS_SM film's enhanced hardness compared to closed field design was related to three factors: high density, small grains, and higher compressive stresses. The increase in stress with smaller grain size generally inhibits dislocation movements.[55] This type of stress inducing hardening has been observed in metal nitrides such as ZrN[49] and NbN.[60] Two factors can be the cause of degradation of hardness in HiPIMS_SM compared to the HiPIMS_CF: (i) stress reduction resulting from a grain size increase and thickness, (b) development of (200) orientation compared to the dominating (111) orientation. Since the Schmid factors were the lowest for applied loads on (111) planes than (001) for NaCl type structures.[61] It is a challenge to indent on this plane as we encounter a large array of tightly packed atoms in the [111] direction. But the inset in Fig. 13(a) shows that films with 111 orientations have lower hardness than those with no orientation or 001 orientations.

This implies that the hardness is primarily determined by the film density (Fig. S4 in the supplementary material)[62] and stress state [Fig. 13(b)], and the stress generation is from the compositional differences in the films. We can group the film hardness into regions "A" and "B" shown in Fig. 13(b). The figure shows that the hardness linearly increases with the residual stress, which is a function of the composition differences. This composition differences were induced by the increased ion bombardment with varying energy due to applied V_{bias}. Similar groupings of hardness were observed as a function of E_r which depends on the density of the films (Fig. S4 in the supplementary material).[62] The hardness has a linear relation with E_r with unique slopes for groups "A" and "B." To summarize, the hardening in DCMS_CF and DCMS_SM was due to stress increase with V_{bias} since density in each of these cases was constant with V_{bias}. However, for HiPIMS_CF deposited films the stress was constant except for the floating bias, and the density contributed to film hardness. For HiPIMS_SM it is both density and stress were responsible for the hardening effect.

The total process energy consumptions of TiZrNbTaN films reported in Ref. 26 was ~0.22 kWh. This included energy used for the cathodes (~0.2 kWh) and substrate heating (~0.02 kWh). The total time required for the deposition of the sample with the best mechanical properties was around ~2.5 h. This included the time required for the temperature stabilization before deposition, deposition time, and cooling. The total process energy consumption in the present work is ~0.24 kWh with a total process time of ~2.3 h for the film with best properties. Even though the total process energy consumption is ~9% higher, there is ~8.5% reduction in process time. Therefore, both techniques are equivalent in terms of

23 November 2023 11:57:08

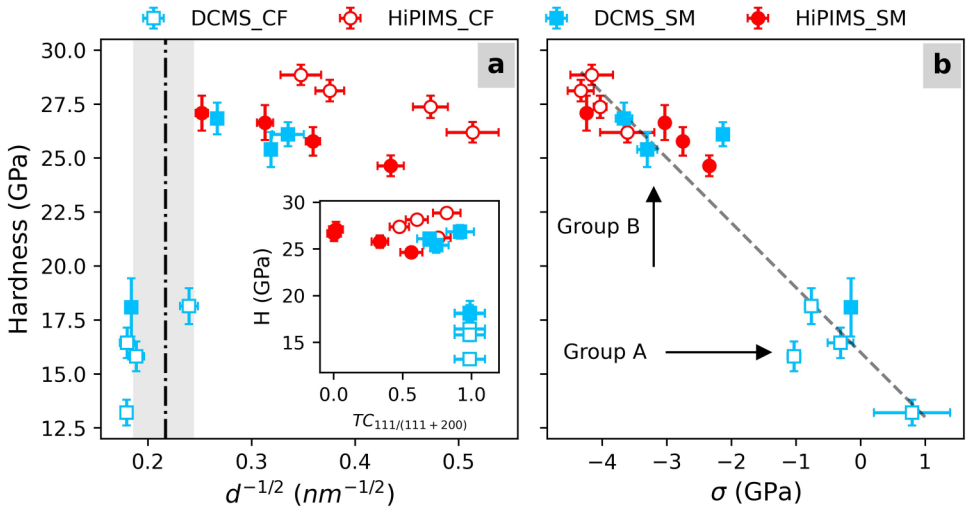

FIG. 13. Hardness of TiZrNbTaN coatings as a function of (a) inverse square root of the grain size. The inset in (a) shows the hardness of the films as a function of the ratio of 111 and 200 texture coefficients and (b) residual stress.

© Author(s) 2023

energy and time usage. In addition, the crystallographic properties were similar for both methods, but further work is needed to have equivalent thickness and stress values.

V. CONCLUSIONS

The effect of the tilted closed field magnetron chamber design with four sources on the properties of TiZrNbTa nitride coatings was investigated. The cross coupling of the magnetic field due to multiple sources had a dramatic influence on the sputtered flux reaching the substrate. The increased ion bombardment at the substrate when deposited with single magnetron had a direct influence on the stress, density, and grain size of the films which impacted the hardness. The mechanical properties improved with an increase in the substrate bias. Films deposited with closed field design using HiPIMS had the highest stress and hardness. Stress reduction and mild degradation in hardness were observed in films grown with single magnetron. The coatings deposited by DCMS with single magnetron had similar stress, density, and hardness as that of HiPIMS one. However, the main difference was observed in the crystallographic orientation that changed from 111 to 200 in HiPIMS single magnetron deposited films. Hence, the magnetron design has a significant effect on the microstructure and mechanical properties of the films. In addition, the TiZrNbTaN films with better mechanical properties can be obtained at room temperature than at higher substrate temperatures.

ACKNOWLEDGMENTS

The work was supported financially by the VINNOVA Competence Centre FunMat-II (Grant No. 2022-03071), the Swedish Government Strategic Research Area in Materials Science on Functional Materials at Linköping University (Faculty Grant SFO-Mat-LiU No. 2009 00971), the Knut and Alice Wallenberg foundation through the Wallenberg Academy Fellows program (KAW-2020.0196), the Swedish Research Council (VR) under Project No. 2021-03826, and the Swedish Energy Agency under Project No. 52740-1.

AUTHOR DECLARATIONS

Conflicts of Interest

The authors have no conflicts to disclose.

Author Contributions

Sanath Kumar Honnali: Conceptualization (equal); Data curation (equal); Formal analysis (equal); Investigation (equal); Software (lead); Writing – original draft (lead). **Charlotte Poterie:** Conceptualization (equal); Data curation (equal); Formal analysis (equal); Investigation (equal). **Arnaud le Febvrier:** Conceptualization (equal); Formal analysis (equal); Writing – review & editing (equal). **Daniel Lundin:** Conceptualization (equal); Funding acquisition (equal); Supervision (equal); Writing – review & editing (equal). **Grzegorz Greczynski:** Funding acquisition (equal); Supervision (equal); Writing – review & editing (equal). **Per Eklund:** Conceptualization (equal); Funding acquisition (equal); Supervision (equal); Writing – review & editing (equal).

DATA AVAILABILITY

The data that support the findings of this study are available from the corresponding author upon reasonable request.

REFERENCES

[1]W. D. Gill and E. Kay, Rev. Sci. Instrum. **36**, 277 (1965).
[2]W. Kiyotaka and H. Shigeru, J. Phys. Soc. Jpn. **21**, 738 (1966).
[3]R. K. Waits, J. Vac. Sci. Technol. **15**, 179 (1978).
[4]J. S. Chapin, "Sputtering process and apparatus," U.S. patent 4,166,018A (1979).
[5]S. D. Ekpe, F. J. Jimenez, D. J. Field, M. J. Davis, and S. K. Dew, J. Vac. Sci. Technol. A **27**, 1275 (2009).
[6]N. Savvides and B. Window, J. Vac. Sci. Technol. A **4**, 504 (1986).
[7]S. L. Rohde, *Plasma Sources Science and Technology*, edited by M. H. Francombe and J. L. Vossen (Elsevier, San Diego, 1994), pp. 235–288.
[8]B. Window and N. Savvides, J. Vac. Sci. Technol. A **4**, 196 (1986).
[9]P. J. Kelly, R. D. Arnell, W. Ahmed, and A. Afzal, Mater. Des. **17**, 215 (1996).
[10]P. J. Kelly and R. D. Arnell, Surf. Coat. Technol. **108–109**, 317 (1998).
[11]W. D. Sproul, P. J. Rudnik, M. E. Graham, and S. L. Rohde, Surf. Coat. Technol. **43–44**, 270 (1990).
[12]D. P. Monaghan, D. G. Teer, K. C. Laing, I. Efeoglu, and R. D. Arnell, Surf. Coat. Technol. **59**, 21 (1993).
[13]P. J. Kelly and R. D. Arnell, Vacuum **56**, 159 (2000).
[14]K. Bobzin, N. Bagcivan, P. Immich, S. Bolz, J. Alami, and R. Cremer, J. Mater. Process. Technol. **209**, 165 (2009).
[15]G. Greczynski *et al.*, Thin Solid Films **556**, 87 (2014).
[16]C. Engström, T. Berlind, J. Birch, L. Hultman, I. P. Ivanov, S. R. Kirkpatrick, and S. Rohde, Vacuum **56**, 107 (2000).
[17]A. le Febvrier, L. Landälv, T. Liersch, D. Sandmark, P. Sandström, and P. Eklund, Vacuum **187**, 110137 (2021).
[18]I. Petrov, A. Myers, J. E. Greene, and J. R. Abelson, J. Vac. Sci. Technol. A **12**, 2846 (1994).
[19]C. Christou and Z. H. Barber, J. Vac. Sci. Technol. A **18**, 2897 (2000).
[20]J. T. Gudmundsson, N. Brenning, D. Lundin, and U. Helmersson, J. Vac. Sci. Technol. A **30**, 030801 (2012).
[21]D. Lundin and K. Sarakinos, J. Mater. Res. **27**, 780 (2012).
[22]J. T. Gudmundsson, Vacuum **84**, 1360 (2010).
[23]S. L. Rohde, I. Petrov, W. D. Sproul, S. A. Barnett, P. J. Rudnik, and M. E. Graham, Thin Solid Films **193–194**, 117 (1990).
[24]S. G. Rao, R. Shu, R. Boyd, A. le Febvrier, and P. Eklund, Vacuum **204**, 111331 (2022).
[25]J. Bohlmark, M. Östbye, M. Lattemann, H. Ljungcrantz, T. Rosell, and U. Helmersson, Thin Solid Films **515**, 1928 (2006).
[26]R. Shu, E.-M. Paschalidou, S. G. Rao, J. Lu, G. Greczynski, E. Lewin, L. Nyholm, A. le Febvrier, and P. Eklund, Surf. Coat. Technol. **389**, 125651 (2020).
[27]R. Shu, D. Lundin, B. Xin, M. A. Sortica, D. Primetzhofer, M. Magnuson, A. le Febvrier, and P. Eklund, ACS Appl. Electron. Mater. **3**, 2748 (2021).
[28]P. Malinovskis, S. Fritze, L. Riekehr, L. von Fieandt, J. Cedervall, D. Rehnlund, L. Nyholm, E. Lewin, and U. Jansson, Mater. Des. **149**, 51 (2018).
[29]R. Shu *et al.*, Surf. Coat. Technol. **426**, 127743 (2021).
[30]S. Fritze, P. Malinovskis, L. Riekehr, L. von Fieandt, E. Lewin, and U. Jansson, Sci. Rep. **8**, 14508 (2018).
[31]M. Ortner and L. G. Coliado Bandeira, SoftwareX **11**, 100466 (2020).
[32]J. D. Hunter, Comput. Sci. Eng. **9**, 90 (2007).
[33]J. D. Jackson and R. F. Fox, Am. J. Phys. **67**, 841 (1999).
[34]G. C. A. M. Janssen, M. M. Abdalla, F. van Keulen, B. R. Pujada, and B. van Venrooy, Thin Solid Films **517**, 1858 (2009).
[35]W. C. Oliver and G. M. Pharr, J. Mater. Res. **7**, 1564 (1992).

23 November 2023 11:57:08

© Author(s) 2023

[36]D. J. Christie, J. Vac. Sci. Technol. A **23**, 330 (2005).
[37]A. Khorsand Zak, W. H. Abd. Majid, M. E. Abrishami, and R. Yousefi, Solid State Sci. **13**, 251 (2011).
[38]P. Paufler, Cryst. Res. Technol. **16**, 982 (1981).
[39]Q. Kong, L. Ji, H. Li, X. Liu, Y. Wang, J. Chen, and H. Zhou, Mater. Sci. Eng., B **176**, 850 (2011).
[40]Z. He, S. Zhang, and D. Sun, Thin Solid Films **676**, 60 (2019).
[41]S. Gangopadhyay, R. Acharya, A. K. Chattopadhyay, and S. Paul, Vacuum **84**, 843 (2010).
[42]S. M. Rossnagel and J. J. Cuomo, Thin Solid Films **171**, 143 (1989).
[43]I. Petrov, P. B. Barna, L. Hultman, and J. E. Greene, J. Vac. Sci. Technol. A **21**, S117 (2003).
[44]J. Pelleg, L. Z. Zevin, S. Lungo, and N. Croitoru, Thin Solid Films **197**, 117 (1991).
[45]U. C. Oh and J. H. Je, J. Appl. Phys. **74**, 1692 (1993).
[46]T. Ogawa, J. Alloys Compd. **203**, 221 (1994).
[47]E. Chason, M. Karlson, J. J. Colin, D. Magnfält, K. Sarakinos, and G. Abadias, J. Appl. Phys. **119**, 145307 (2016).
[48]L. Zhang, H. Yang, X. Pang, K. Gao, and A. A. Volinsky, Surf. Coat. Technol. **224**, 120 (2013).
[49]Z. B. Qi, P. Sun, F. P. Zhu, Z. C. Wang, D. L. Peng, and C. H. Wu, Surf. Coat. Technol. **205**, 3692 (2011).
[50]H. Conrad and J. Narayan, Scr. Mater. **42**, 1025 (2000).
[51]W. He, S. D. Bhole, and D. Chen, Sci. Technol. Adv. Mater. **9**, 015003 (2008).
[52]A. Cavaleiro, B. Trindade, and M. T. Vieira, in *Nanostructured Coatings*, edited by A. Cavaleiro, J. T. M. De Hosson (Springer, New York, 2006), pp. 261–314.
[53]J. D. Eshelby, F. C. Frank, and F. R. N. Nabarro, London, Edinburgh Dublin Philos. Mag. J. Sci. **42**, 351 (1951).
[54]C.-H. Ma, J.-H. Huang, and H. Chen, Surf. Coat. Technol. **200**, 3868 (2006).
[55]P. H. Mayrhofer, C. Mitterer, L. Hultman, and H. Clemens, Prog. Mater. Sci. **51**, 1032 (2006).
[56]H. Windischmann, J. Appl. Phys. **62**, 1800 (1987).
[57]F. M. D'Heurle and J. M. E. Harper, Thin Solid Films **171**, 81 (1989).
[58]H. Oettel, R. Wiedemann, and S. Preißler, Surf. Coat. Technol. **74–75**, 273 (1995).
[59]M. Hakamada, Y. Nakamoto, H. Matsumoto, H. Iwasaki, Y. Chen, H. Kusuda, and M. Mabuchi, Mater. Sci. Eng., A **457**, 120 (2007).
[60]M. Wen, C. Q. Hu, C. Wang, T. An, Y. D. Su, Q. N. Meng, and W. T. Zheng, J. Appl. Phys. **104**, 023527 (2008).
[61]H. Ljungcrantz, M. Odén, L. Hultman, J. E. Greene, and J. E. Sundgren, J. Appl. Phys. **80**, 6725 (1996).
[62]See supplementary material online for the details regarding the magnetic field simulations (Fig. S1), lattice parameter [Fig. S2(a)], film thickness [Fig. S2(b)], film composition (Fig. S3), and mechanical properties (Fig. S4) of TiZrNbTaN coatings.

23 November 2023 11:57:08

© Author(s) 2023